

Article

# An Improved Multi-Objective Particle Swarm Optimization Method for Rotor Airfoil Design

Yongchuan Wu<sup>1</sup>, Gang Sun<sup>1</sup> and Jun Tao<sup>1,2,\*</sup>

<sup>1</sup> Department of Aeronautics & Astronautics, Fudan University, Shanghai 200433, China; 20210290012@fudan.edu.cn (Y.W.); gang\_sun@fudan.edu.cn (G.S.)

<sup>2</sup> Rotor Aerodynamics Key Laboratory, China Aerodynamics Research and Development Center, Mianyang 621000, China

\* Correspondence: juntao@fudan.edu.cn

**Abstract:** In this study, a multi-objective aerodynamic optimization is performed on the rotor airfoil via an improved MOPSO (multi-objective particle swarm optimization) method. A database of rotor airfoils containing both geometric and aerodynamic parameters is established, where the geometric parameters are obtained via the CST (class shape transformation) method and the aerodynamic parameters are obtained via CFD (computational fluid dynamics) simulations. On the basis of the database, a DBN (deep belief network) surrogate model is proposed and trained to accurately predict the aerodynamic parameters of the rotor airfoils. In order to improve the convergence rate and global searching ability of the standard MOPSO algorithm, an improved MOPSO framework is established. By embedding the DBN surrogate model into the improved MOPSO framework, multi-objective and multi-constraint aerodynamic optimization for the rotor airfoil is performed. Finally, the aerodynamic performance of the optimized rotor airfoil is validated through CFD simulations. The results indicate that the aerodynamic performance of the optimized rotor airfoil is improved dramatically compared with the baseline rotor airfoil.

**Keywords:** rotor airfoil; aerodynamic; improved MOPSO algorithm; deep belief network



**Citation:** Wu, Y.; Sun, G.; Tao, J. An Improved Multi-Objective Particle Swarm Optimization Method for Rotor Airfoil Design. *Aerospace* **2023**, *10*, 820. <https://doi.org/10.3390/aerospace10090820>

Academic Editor: Anthony D. Gardner

Received: 10 August 2023

Revised: 14 September 2023

Accepted: 14 September 2023

Published: 20 September 2023



**Copyright:** © 2023 by the authors. Licensee MDPI, Basel, Switzerland. This article is an open access article distributed under the terms and conditions of the Creative Commons Attribution (CC BY) license (<https://creativecommons.org/licenses/by/4.0/>).

## 1. Introduction

The rotor is one of the key aerodynamic parts of a helicopter, and its aerodynamic characteristics determine the flight performance of a helicopter to a great extent. The rotor airfoil is the elementary component of the rotor, so its aerodynamic performance is closely related to that of the rotor and effectively influences the performance of helicopters. Therefore, aerodynamic optimization of the rotor airfoil is of critical importance for improving the aerodynamic performance of helicopters, and numerous studies on rotor airfoil design have been conducted by researchers from all over the world. Since the 1970s, research institutions such as NASA, ONERA, and Boeing have developed a series of advanced rotor airfoils such as the OA series [1], VR series [2], and TsAGI series [3], and the performance of helicopters has been improved significantly. Vu et al. [4] made use of the SQP (sequence quadratic program) method and the Kriging surrogate model to optimize the rotor blade airfoil in a hovering state. Tatossian et al. [5] conducted rotor airfoil optimization based on the NACA23013 airfoil via control theory under forward flight state, and the results proved to be beneficial. Yu et al. [6] conducted dynamic stall optimization on the rotor airfoil via a differential evolution algorithm and the Kriging surrogate model and compared the optimized results by the differential evolution algorithm with those by the adjoint method. The comparison indicated that the lift performance of the rotor airfoil obtained by the differential evolution algorithm was better.

Furthermore, helicopters usually work under multiple operating states such as hovering, maneuvering, and forward flight, which makes the aerodynamic optimization of the rotor airfoil a multi-objective and multi-constraint issue. Yang et al. [7] conducted a

multi-objective optimization on the rotor airfoil by weighting the drag under hovering, the lift under maneuvering, and the drag at the divergence Mach number into a single objective. Wang et al. [8] combined multiple design objectives into a single objective and conducted the multi-objective optimization of the SC1095 airfoil via GA (genetic algorithm). However, the optimization results of the objective weighting methods highly depend on the selection of weight factors, which may be unable to avoid the solutions in extreme situations. Thus, multi-objective optimization algorithms appear especially important for the aerodynamic optimization of rotor airfoils. In multi-objective optimizations, the multi-objectives are not independent but coupled together and competing with each other, so the solution for the multi-objective optimization problem is not one single solution but a group of equilibrium solutions, known as the Pareto optimal solution set, which makes the multi-objective optimization more complex and difficult. Therefore, the efficiency of the multi-objective optimization is lower than that of the single-objective optimization because the multi-objectives need to be balanced in multi-objective optimizations, and it takes time to deal with the Pareto set in each iteration. Many multi-objective optimization algorithms have been developed over the past few decades, such as MOGA (multi-objective genetic algorithm) [9], MOPSO (multi-objective particle swarm optimization) [10], etc. Most of these multi-objective optimization algorithms have been applied in the aerodynamic optimization of rotor airfoils [11–14]. However, there still exist some limitations with these multi-objective optimization algorithms. For instance, it is difficult for MOGA to generate a complete Pareto optimal set due to the complexity of its own application and the limited size of the calculus group [15]. The MOPSO algorithm has the defects of low convergence rate and poor diversity of solutions, which lead to a local optimum easily in the late iterations [16]. Thus, it is necessary to improve the efficiency of the current multi-objective optimization algorithms.

For conventional multi-objective optimization of a rotor airfoil, the multi-objective functions are evaluated via CFD simulations in each iteration of the optimization process, and it could be very time consuming. In order to improve the optimization efficiency, surrogate models are expected to replace the CFD simulations and can play an important role. Surrogate models, such as Kriging [17], BP (backpropagation) neural network [18], etc., have been proposed and developed in the past few decades. However, these conventional surrogate models are still not accurate enough [19], so surrogate models with higher accuracy need to be investigated and developed.

Given the above, aerodynamic optimization of the rotor airfoil is of great significance, and it is a multi-objective and multi-constraint problem. In this study, the airfoil in the middle of the rotor blade for a medium transport helicopter is optimized under different operating states, namely hovering, maneuvering, and forward flight, and the different operating states correspond to different Mach numbers for the rotor airfoil. In order to improve the efficiency of the multi-objective optimization for the rotor airfoil, a multi-objective optimization framework based on the deep learning surrogate model and the improved MOPSO algorithm is developed. Firstly, a database of rotor airfoils is established with geometric parameters obtained via the CST method and aerodynamic parameters obtained via CFD simulations. Based on the database, a DBN (deep belief network) surrogate model is proposed and trained for the purpose of accurately predicting the aerodynamic parameters of the rotor airfoils. In order to improve the convergence rate and global searching ability of the standard MOPSO algorithm, an improved MOPSO algorithm is proposed. Then, an improved MOPSO framework is established by coupling the improved MOPSO algorithm and the DBN surrogate model. Finally, a multi-objective aerodynamic optimization for the rotor airfoil under constraints is performed via the improved MOPSO framework, and the aerodynamic parameters of the optimized rotor airfoil are validated via CFD simulations.

The remainder of this paper is organized as follows. In Section 2, the numerical methods and validations are performed. In Section 3, the optimization framework for the rotor airfoil is established and introduced. In Section 4, the optimization results are

presented and analyzed. Finally, in Section 5, some conclusions are drawn according to the previous results and analyses.

## 2. Numerical Methods and Validations

In this study, the aerodynamic parameters of the rotor airfoils are obtained through solving the RANS (Reynolds-Averaged Navier-Stokes) equations. An in-house CFD code named FDNS Solver is used for CFD simulations. The Roe-FDS method [20] is employed in space discretization while an implicit LU-SGS method [20] is adopted in time discretization. The one-equation S-A (Spalart-Allmaras) turbulence model [21] is adopted for turbulence simulation.

In order to verify the reliability of the CFD method, numerical simulations are conducted on the NACA 0012 airfoil, then the computational results are compared with the experimental ones. The grid number of the entire computational domain is about  $2.5 \times 10^5$ . The computational conditions are set as:  $Ma = 0.3$ ,  $Re = 6 \times 10^6$ .

Figure 1 shows the comparison of the pressure coefficients between the computational results and the experimental ones [22] at the AoA (angle of attack) of  $9.86^\circ$ . As can be seen, the computational results of pressure coefficients agree well with the experimental ones.

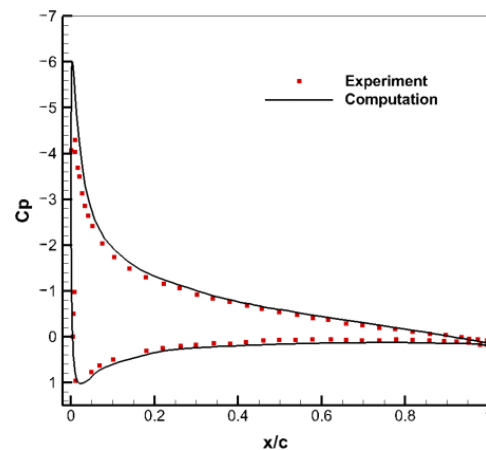


Figure 1. Comparison of the pressure coefficients for NACA 0012 airfoil (AoA =  $9.86^\circ$ ).

Figure 2 shows the computational lift and drag curves compared with the experimental ones [23]. As can be seen, the computational curves are basically in accordance with the experimental ones for both lift and drag coefficients. Thus, from the above comparison results, it can be concluded that the CFD method is reliable for evaluating the aerodynamic coefficients.

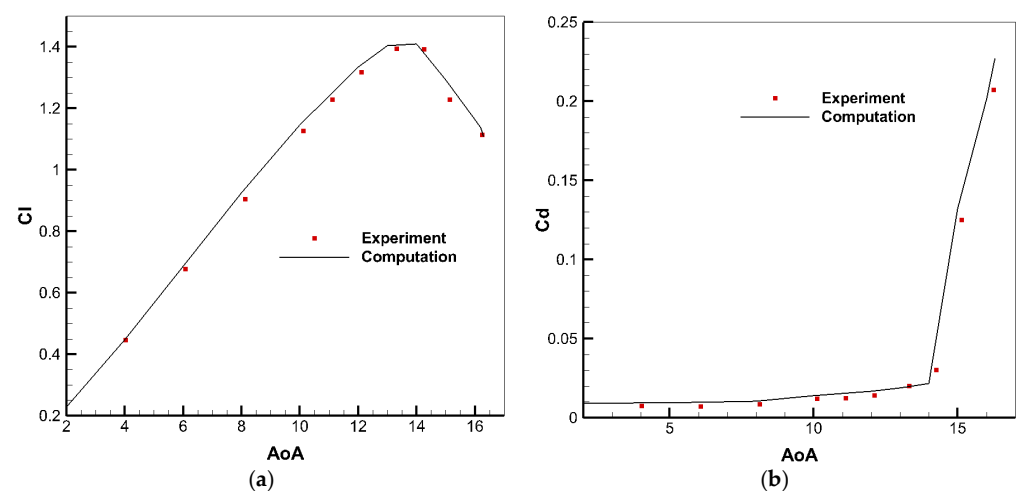


Figure 2. Comparison of lift and drag curves for NACA 0012 airfoil. (a) Lift curve. (b) Drag curve.

### 3. Optimization Framework for Rotor Airfoil Optimization

This study focuses on optimizing an airfoil in the middle of the rotor blade for a medium transport helicopter under different operating states, namely hovering, maneuvering, and forward flight, which makes it a multi-objective optimization issue. The DBN surrogate model is proposed to accurately predict the aerodynamic parameters of the rotor airfoils, and the improved MOPSO framework is developed to improve the convergence rate and global searching ability of the standard MOPSO algorithm. Through the study of 2D airfoil optimization, the feasibility of this surrogate-model-based optimization method is verified, which lays the foundation for the subsequent study of 3D rotor-blade optimization. In this study, the algorithms such as surrogate models and optimization algorithms are implemented via Matlab 2023a.

#### 3.1. Parameterization Method

The parameterization method determines the number of the design variables. For airfoil optimization, the parameterization method should describe the geometry of the airfoil with as few characteristic parameters as possible in order to reduce the number of design variables.

In this study, the CST method [24], which uses class function and shape function to represent geometric characteristics, is employed to parameterize the geometry of the rotor airfoil. As for the CST method, the upper and lower surfaces are defined as the product of a class function, a shape function, and a linear term of tail thickness, where the class function represents the geometric type to be described, and the shape function modifies the geometric properties on the basis of the class function. The CST parameterization method can be described as follows:

$$\left\{ \begin{array}{l} y_u = C_{N_2}^{N_1}(x)S_u(x) + xy_{teu} \\ y_l = C_{N_2}^{N_1}(x)S_l(x) + xy_{tel} \\ C_{N_2}^{N_1}(x) = x^{N_1}(1-x)^{N_2} \\ S_u(x) = \sum_{i=0}^{nu} A_u(i) \frac{nu!}{i!(nu-i)!} x^i (1-x)^{nu-i} \\ S_l(x) = \sum_{i=0}^{nl} A_l(i) \frac{nl!}{i!(nl-i)!} x^i (1-x)^{nl-i} \end{array} \right. \quad (1)$$

where  $x$ ,  $y_u$ , and  $y_l$  represent the  $x$  coordinate, the  $y$  coordinate on the upper surface, and the  $y$  coordinate on the lower surface, respectively.  $y_{teu}$  and  $y_{tel}$  are the  $y$  coordinate of the trailing edge on the upper surface and the  $y$  coordinate of the trailing edge on the lower surface, respectively.  $C_{N_2}^{N_1}(x)$  is the class function, where  $N_1$  and  $N_2$  are set to be 0.5 and 1.0, respectively, in this study.  $S_u(x)$  and  $S_l(x)$  are shape functions, while  $nu$  and  $nl$  are the orders of the polynomials for the upper surface and the lower surface, respectively.  $A_u(i)$  ( $i = 0, 1, \dots, nu$ ) and  $A_l(i)$  ( $i = 0, 1, \dots, nl$ ) are the coefficient vectors corresponding to the shape functions. For airfoil optimization,  $A_u(i)$  ( $i = 0, 1, \dots, nu$ ) and  $A_l(i)$  ( $i = 0, 1, \dots, nl$ ) are the design variables, and the orders of the polynomials for both the upper and lower surfaces are set to be 6 ( $nu = nl = 6$ ) in this study, thus the number of the design variables for the rotor airfoil optimization is 14.

In order to test the accuracy of the CST method, parameterization is conducted for the baseline rotor airfoil that was obtained in our previous design. Figure 3 shows the parameterized shape of the baseline airfoil by the CST method compared with the original shape. Figure 4 shows the fitting residual of the CST parameterized airfoil at each  $x$  coordinate, where the range of  $x/c$  from  $-1$  to  $0$  represents the upper surface, and that from  $0$  to  $1$  represents the lower surface. As can be seen, the parameterized shape by the CST method is basically in accordance with the original one, and the residuals are all less than  $2 \times 10^{-3}$ , which indicates that the CST method adopted in this study is highly reliable in describing the geometry of the airfoil.

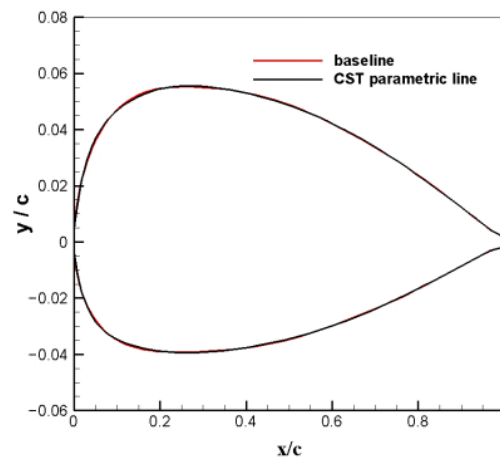


**Figure 3.** Comparison of the baseline airfoil between the CST parameterized shape and the original one.

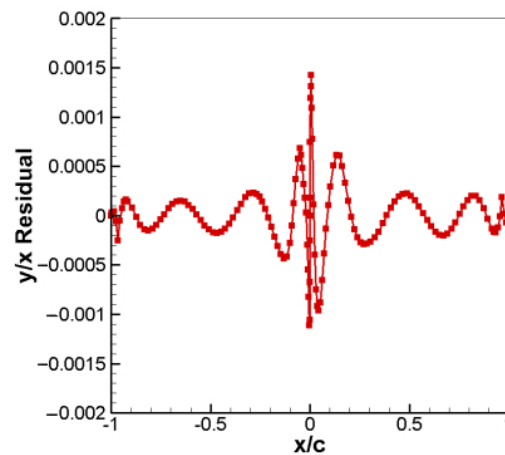


**Figure 4.** Fitting residuals of the CST parameterized airfoil.

### 3.2. Deep Learning-Based Surrogate Model

Deep learning usually refers to the method of a multi-layer artificial neural network. In recent years, deep learning methods have been studied more and more by scientists from all over the world and have been applied in widespread fields [25]. Due to employing particular mathematical operations and activation functions, deep learning methods have demonstrated tremendous potential in extracting information and fitting nonlinear functions. Given this, in order to improve the efficiency of the optimization and the accuracy of predicting the aerodynamic performance, DBN [26] is introduced as the surrogate model during the optimization process of the rotor airfoil in this study.

As a typical deep learning method, DBN is a probability generative model, and its basic component is the RBM (restricted Boltzmann machine). Figure 5 shows the typical network structure of the RBM.

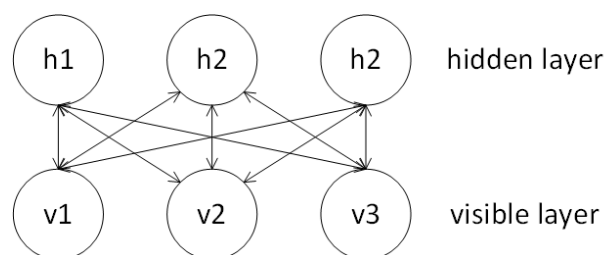


**Figure 5.** Structure of the RBM.

An RBM is composed of a visible layer and a hidden layer. The visible layer is composed of visible units for data input, while the hidden layer is composed of hidden units for feature detection. The two layers of neurons in an RBM are symmetrically connected, and the neurons in the same layer are independent of each other. The connection between the visible layers and the hidden layers can be represented by a weight matrix. Assuming that the visible layer has  $M$  neurons and the hidden layer has  $N$  neurons, the weight matrix then can be expressed as follows:

$$W = \begin{bmatrix} w_{1,1} & w_{2,1} & \dots & w_{M,1} \\ w_{1,2} & w_{2,2} & \dots & w_{M,2} \\ \dots & \dots & \dots & \dots \\ w_{1,N} & w_{2,N} & \dots & w_{M,N} \end{bmatrix} \quad (2)$$

where  $w_{i,j}$  represents the weight from the  $i$ -th visible neuron to the  $j$ -th hidden neuron.

Figure 6 shows the structure of the DBN. The DBN is constructed by connecting multiple RBMs in series; the hidden layer of the previous RBM is taken as the visible layer of the next RBM. The RBMs are trained layer by layer forward via unsupervised learning to preliminarily construct the DBN, and this procedure is also called the pre-training of the DBN. After the pre-training, the initial weight values are obtained. Then a BP neural network [18] is set between the last two layers of the DBN, the weights of the entire network are tuned backward in a supervised manner, and this procedure is also called the fine-tuning of the DBN.

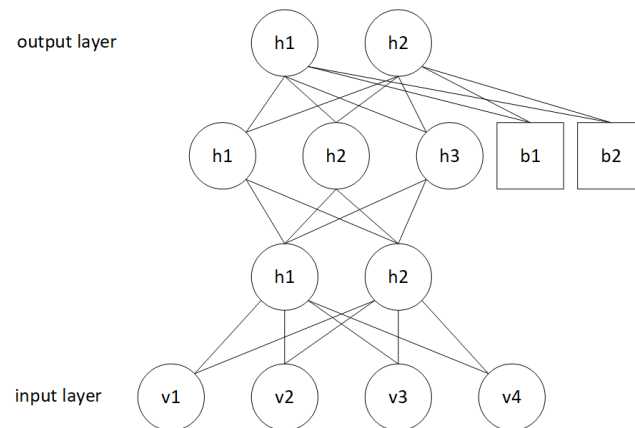


**Figure 6.** Structure of the DBN.

In this study, the input layer of the DBN represents the design variables by the CST method, while the output layer of the DBN represents the aerodynamic parameters. By employing RBMs, DBN overcomes the shortcomings of the BP network that it traps into local optimums easily.

### 3.3. The Improved MOPSO Algorithm

In this study, an improved MOPSO algorithm is employed for the multi-objective optimization of the rotor airfoil. The initial PSO (particle swarm optimization) algorithm [27] is a single-objective optimization algorithm that derives from the research of birds searching for food. Each bird is taken as a particle. The position of the particle is taken as a candidate solution of the problem, and the objective function value corresponding to the candidate solution is called fitness. During the optimization process, the position of the particle with the best fitness is the optimal position of the swarm. For each particle, the position with the best fitness in the search history is called the historical optimal position of the particle.

The velocity of each particle can be adjusted based on the historical optimal position of the particle and the optimal position of the swarm, and this process is also called evolution.

Then, the optimal solution can be updated after the evolution. The evolution equation for the velocity and position of each particle is expressed as follows:

$$\begin{aligned} V_i(k+1) &= wV_i(k) + c_1r_1(P_{best}[i] - A_i) + c_2r_2(P_{best}[g] - A_i) \\ A_i(k+1) &= A_i(k) + KV_i(k+1) \end{aligned} \quad (3)$$

where  $w$  is the inertia weight,  $c_1$  and  $c_2$  are the acceleration factors,  $r_1$  and  $r_2$  are random numbers between 0 and 1.  $K$  is the compression factor, which is used to constrain the flight speeds of the particles.  $P_{best}[i]$  is the historical optimal position of a single particle, while  $P_{best}[g]$  is the best position of the swarm.

The MOPSO algorithm was first proposed by Coello [28] for multi-objective optimization problems. Based on it, Raqual [29] put forward the CDMOPSO (crowding distance multi-objective particle swarm optimization) algorithm, which introduced the repository of non-dominated solutions and crowding distances of particles to improve the diversity of the swarm. Crowding distance is a parameter that estimates the density of other solutions around one solution. For each objective function, the solutions in the external elite solution set are categorized according to the value of the objective function, and then the average side length of the cube formed by two particles adjacent to each solution is calculated as shown in Figure 7. The final result is the crowding distance of this solution, and the crowding distances of the particles can reflect the diversity of the solutions.

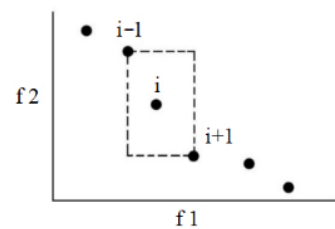


**Figure 7.** Schematic of the crowding distance.

In this study, in order to enhance the convergence rate and global searching ability, the  $\alpha$ -stable family of functions [30] is introduced to improve the standard MOPSO algorithm. In the  $\alpha$ -stable family of functions, the stability coefficient  $\alpha$  is an important parameter describing the size of the distribution wake, which determines the distribution range of the generated random numbers. Figure 8 shows the  $\alpha$ -stable distribution under different  $\alpha$  values. By introducing the  $\alpha$ -stable distribution, random numbers are generated during the iterative process of MOPSO, so that the particles are mutated to avoid falling into local optimums too early.

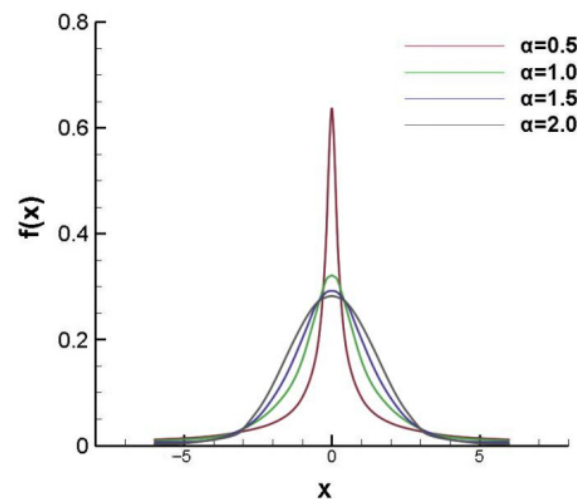


**Figure 8.** Schematic of the  $\alpha$ -stable distribution under different  $\alpha$  values.

Figure 9 shows the flowchart of the ASMOPSO ( $\alpha$ -stable MOPSO) algorithm. The improved MOPSO algorithm is implemented as follows:

- (1) Set the parameters of the particle swarm, including the swarm scale  $N$ , repository capacity  $N_{rep}$ , inertia coefficient  $\omega$ , acceleration factors  $c_1$  and  $c_2$ , mutation probability  $P_{mut}$ , and the maximum number of iteration steps.
- (2) Initialize the positions and velocities of the particles, calculate the fitness, and obtain the optimal position.
- (3) Set  $t = 0$ . The particles in the group are compared by Pareto to get all non-dominated solutions, which are stored in the repository.
- (4) Calculate the crowding distances of the non-dominated solutions in the repository and put them in descending order by the crowding distance.
- (5) Select one of the non-dominated solutions from the repository at the top of a certain proportion as the group optimal position  $P_{best}[g]$ , then update the particle velocities and positions, and make the constraint judgment and mutation with the  $\alpha$ -stable distribution.
- (6) Compare all particles by Pareto, compare the new non-dominated particles with the particles in the repository, and delete the dominated particle in the repository. If the number of non-dominated particles in the repository is equal to the repository capacity  $N_{rep}$ , the particles in the repository are arranged in descending order by the crowding distance, then one of the most crowded areas (e.g., 10% of the minimum crowding distance values) is randomly selected and replaced by the new non-dominated solutions.
- (7) If the current iterative step number is greater than the maximum number of iterative steps, or the precision requirement is reached, then the iteration is terminated, otherwise, return to step 4.

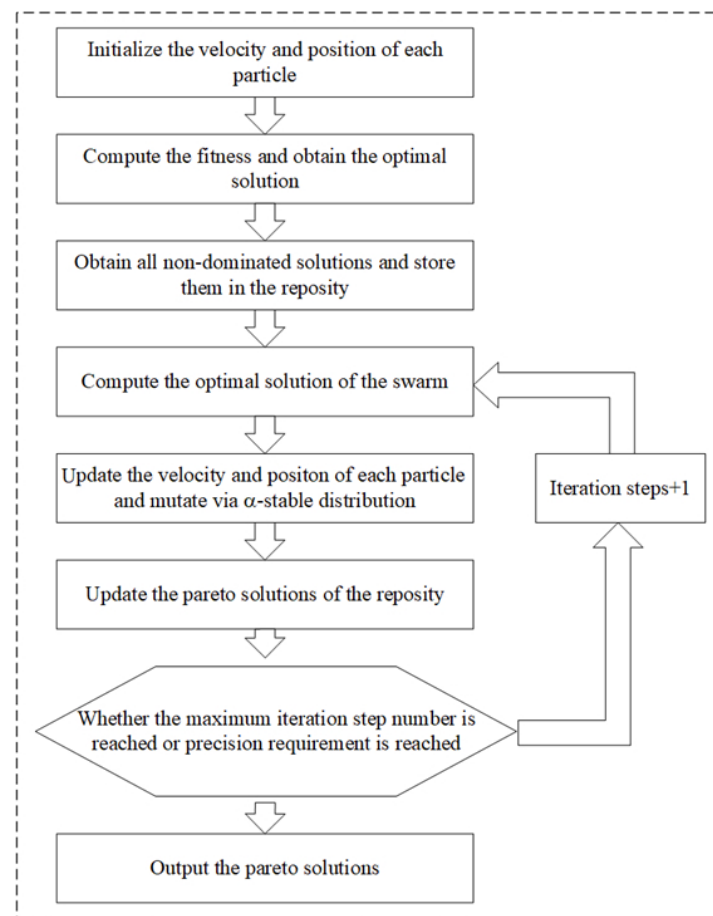


Figure 9. Flowchart of the  $\alpha$ -stable MOPSO algorithm.

In order to compare the performance of CDMOPSO and ASMOPSO, the objective function ZDT3 is used for the test. The IGD (inverted generation distance) is used to comprehensively evaluate the performance of the algorithms. IGD can not only evaluate the convergence of the multi-objective solution set but also evaluate the distribution characteristics of the solution set.

$$A_{IGD} = \frac{\sum_{v \in P^*} d(v, P)}{P^*} \tag{4}$$

where,  $d(v, P)$  is the minimum Euclidean distance between the individual in the approximate solution set  $P$  and the individual  $v$  in the exact solution set  $P^*$ . The optimal solution set obtained by this algorithm is denoted by  $P$ . The lower the value of IGD is, the better the optimization result and the algorithm performance will be.

The function ZDT3 can be described as:

$$\begin{cases} \min f_1(x) = x_1 \\ \min f_2(x) = g \left( 1 - \sqrt{\frac{f_1}{g}} - \left(\frac{f_1}{g}\right) \sin(10\pi f_1) \right) \\ g(x) = 1 + 9 \sum_{i=2}^n \frac{x_i}{n-1} \end{cases} \tag{5}$$

where  $x$  is a 30-dimensional variable, of which the range is  $[0, 1]$ , and  $n = 30$ .

The ZDT3 is independently evaluated 30 times by the CDMOPSO algorithm and the ASMOPSO algorithm. The statistics of the IGD values are shown in Table 1.

**Table 1.** Comparison of the IGD values between the CDMOPSO algorithm and the ASMOPSO algorithm.

	Mean	Variance
CDMOPSO	$5.661 \times 10^{-2}$	$2.946 \times 10^{-3}$
ASMOPSO	$3.300 \times 10^{-2}$	$1.623 \times 10^{-3}$

As can be seen, the IGD values of the ASMOPSO algorithm are lower than those of the CDMOPSO algorithm. Therefore, it can be concluded that the performance of the ASMOPSO algorithm is better than that of the CDMOPSO algorithm for this problem.

### 3.4. EI Infilling Criterion

During the optimization process, the EI (expected improvement) infilling criterion [31–33] is adopted to update the surrogate model in each iteration before the optimization is converged. The expected improvement is taken as the fitness function of the surrogate optimization, and the point with the maximum EI is added to the samples to update the surrogate model in each iteration.

The multi-objective EI is defined as:

$$EI(x) = \int_{y \in R^m} I(x) \prod_{i=1}^m \frac{1}{s_i} \varphi \left( \frac{y_i - \hat{y}_i}{s_i} \right) dy_i \tag{6}$$

where  $\hat{y}_i$  and  $s_i$  are the prediction and the square root of variance value of a concerned point  $x$ ,  $\varphi$  is the Gaussian probability density function, and  $R^m$  is the objective space.

The sub-optimization problem can be described as:

$$\begin{cases} \max EI(x) \\ s.t. \begin{cases} Cd_{maneuvering} \leq Cd_{maneuvering-original} \\ Cd_{hovering} \leq Cd_{hovering-original} \\ Cd_{forwardflight} \leq Cd_{forwardflight-original} \\ 9\% \leq thickness \leq 14\% \end{cases} \end{cases} \tag{7}$$

In each iteration, the point with the maximum EI is selected for CFD simulations to obtain aerodynamic parameters and added to the samples to update the surrogate models.

The termination criterion for the whole optimization is that the maximum differences of the function values of the latest 10 generations are all less than 0.01%. In each iteration, if the termination criterion is satisfied, then the optimization ends, otherwise the iteration continues.

#### 4. Results and Analyses

##### 4.1. Training Results of the DBN Surrogate Model

Based on the CST parameters of the baseline rotor airfoil, 300 groups of the CST parameters are generated via the LHS (Latin hypercube sampling) method [34] by perturbing the CST parameters in the range of [0.8, 1.2] multiples of the original parameters of the baseline airfoil. Then a database containing the geometric parameters and aerodynamic parameters of the 300 airfoils are obtained. The geometric parameters are the CST parameters of each airfoil denoted as [Au0, Au1, Au2, Au3, Au4, Au5, Au6, Al0, Al1, Al2, Al3, Al4, Al5, and Al6], while the aerodynamic parameters are the lift and drag coefficients of each airfoil obtained by CFD simulations under the maneuvering, hovering and forward flight states, denoted as [ $C_{l_{\text{maneuvering}}}$ ,  $C_{d_{\text{maneuvering}}}$ ,  $C_{l_{\text{hovering}}}$ ,  $C_{d_{\text{hovering}}}$ ,  $C_{l_{\text{forward flight}}}$ , and  $C_{d_{\text{forward flight}}}$ ]. As the airfoil is located in the middle of the rotor blade for a medium transport helicopter, according to the design requirements, the computational conditions for the three operating states are shown in Table 2.

**Table 2.** Computational conditions for the three different operating states.

Operating Conditions	Ma	AoA	Re
Maneuvering	0.4	9°	$2.084 \times 10^6$
Hovering	0.6	3.23°	$3.126 \times 10^6$
Forward flight	0.7	3°	$3.647 \times 10^6$

For the purpose of training the DBN surrogate model and validating the accuracy of the DBN surrogate model, 270 airfoils in the database are selected randomly as the training samples, and the remaining 30 airfoils are taken as the test samples. The DBN is constructed with 4 layers of RBMs and trained with the geometric parameters as the input and the aerodynamic parameters as the output. After the pre-training, the weight values are initialized and the output of the last RBM is taken as the input of the BP neural network at the last two layers. Figure 10 shows the training results of the DBN surrogate model, where Y is the expected output and T is the DBN output. As can be seen, the correlation coefficient R is 0.99785, which is extremely close to 1.

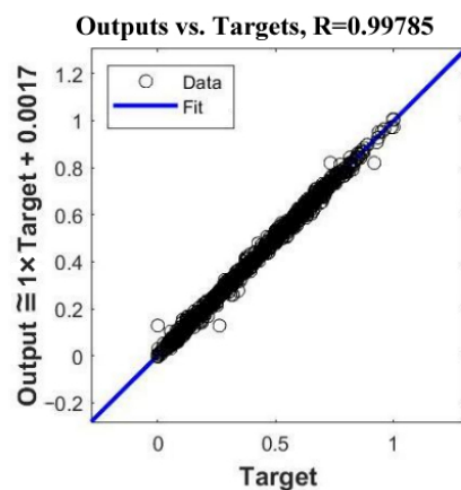


**Figure 10.** Training results of the DBN surrogate model.

Furthermore, in order to compare the performance of the DBN surrogate model and the conventional surrogate models, a BP surrogate model and a Kriging surrogate model are trained and tested using the same training and test samples. Figure 11 shows the predicted lift coefficients by the Kriging model, BP model, and DBN model compared with those by the CFD simulations for the 30 test samples. Figure 12 shows the predicted drag coefficients by the Kriging model, BP model, and DBN model compared with those by the CFD simulations for the 30 test samples. As can be seen, the predicted results by the Kriging model and the BP model are generally in accordance with those by the CFD simulations but differ obviously from the CFD results for some certain test samples. Whereas, the predicted results by the DBN model are close to those by the CFD simulations.

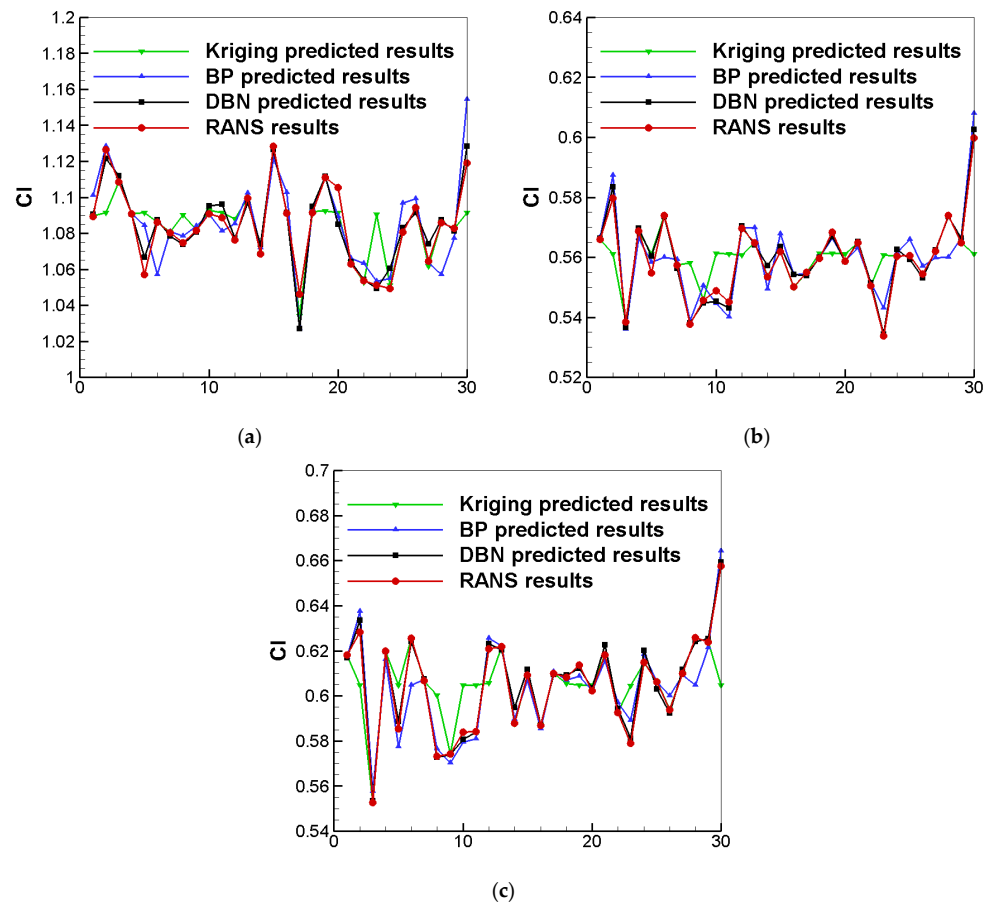


**Figure 11.** Predicted lift coefficients by the Kriging model, BP model, and DBN model compared with CFD results for the test samples. (a) maneuvering. (b) hovering. (c) forward flight.

Table 3 shows the average errors of the aerodynamic parameters predicted by the three surrogate models with respect to the results obtained by CFD simulations for the test samples. The average error of the lift coefficients predicted by the DBN model is 0.3416% for the test samples, while the average errors of the lift coefficients are 0.7597% and 0.9482% for the BP model and Kriging model, respectively. The average error of the drag coefficients predicted by the DBN model is 1.2875% for the test samples, while the average errors of the drag coefficients are 2.5570% and 2.6005% for the BP model and Kriging model, respectively. The errors of the DBN model are significantly smaller than those of the BP model and Kriging model.

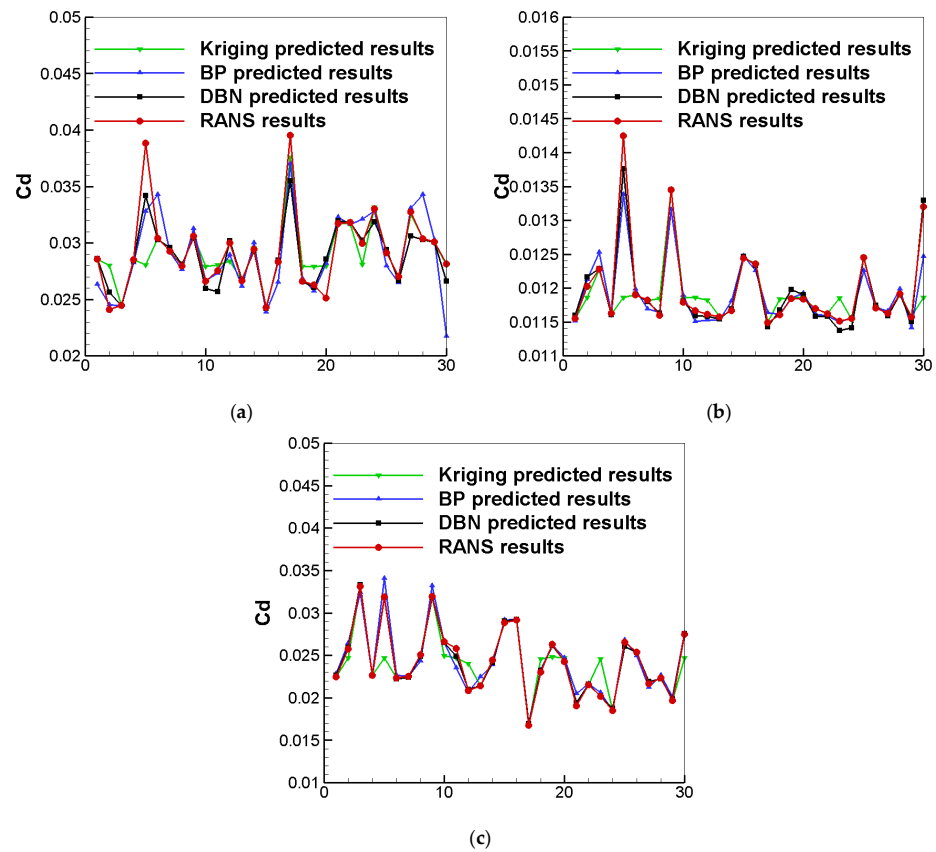


**Figure 12.** Predicted drag coefficients by the Kriging model, BP model, and DBN model compared with CFD results for the test samples. (a) maneuvering. (b) hovering. (c) forward flight.

**Table 3.** Average errors of the aerodynamic parameters predicted by the three surrogate models with respect to the results obtained by CFD simulations for the test samples.

Error [%]	$C_{l_{maneuvering}}$	$C_{d_{maneuvering}}$	$C_{l_{hovering}}$	$C_{d_{hovering}}$	$C_{l_{forward\ flight}}$	$C_{d_{forward\ flight}}$	$C_{l_{overall}}$	$C_{d_{overall}}$
DBN	0.4109	2.5743	0.2815	0.5410	0.3324	0.7473	0.3416	1.2875
BP	0.8220	4.4571	0.7012	1.0738	0.7559	2.1401	0.7597	2.5570
Kriging	0.6819	3.1083	0.9510	1.3678	1.2118	3.3256	0.9482	2.6005

Therefore, from the above results, the DBN surrogate model established in this study is highly reliable in predicting aerodynamic parameters for airfoil optimization, and more accurate than the conventional BP surrogate model and Kriging surrogate model.

#### 4.2. Optimization Results and Analyses

In this study, the multi-objective optimization for the rotor airfoil can be described as follows:

$$\begin{cases} \max C_{l_{maneuvering}}, C_{l_{hovering}}, C_{l_{forwardflight}} \\ s.t. \begin{cases} C_{d_{maneuvering}} \leq C_{d_{maneuvering-original}} \\ C_{d_{hovering}} \leq C_{d_{hovering-original}} \\ C_{d_{forwardflight}} \leq C_{d_{forwardflight-original}} \\ 9\% \leq \text{thickness} \leq 14\% \end{cases} \end{cases} \quad (8)$$

where the thickness is constrained within the range of [9%, 14%] according to the design requirements.

For the purpose of verifying the performance of the ASMOPSO algorithm, optimizations employing the CDMOPSO algorithm and the ASMOPSO algorithm are performed,

respectively. For each optimization, the number of particles is set to 100, the number of Pareto solutions is set to 10, and the mutation rate is set to 0.8.

Figure 13 shows the comparison of the performance between the ASMOPSO algorithm and the CDMOPSO algorithm. As can be seen, the optimization based on the CDMOPSO algorithm converges at the 56th step, while the optimization based on the ASMOPSO algorithm converges at the 44th step.

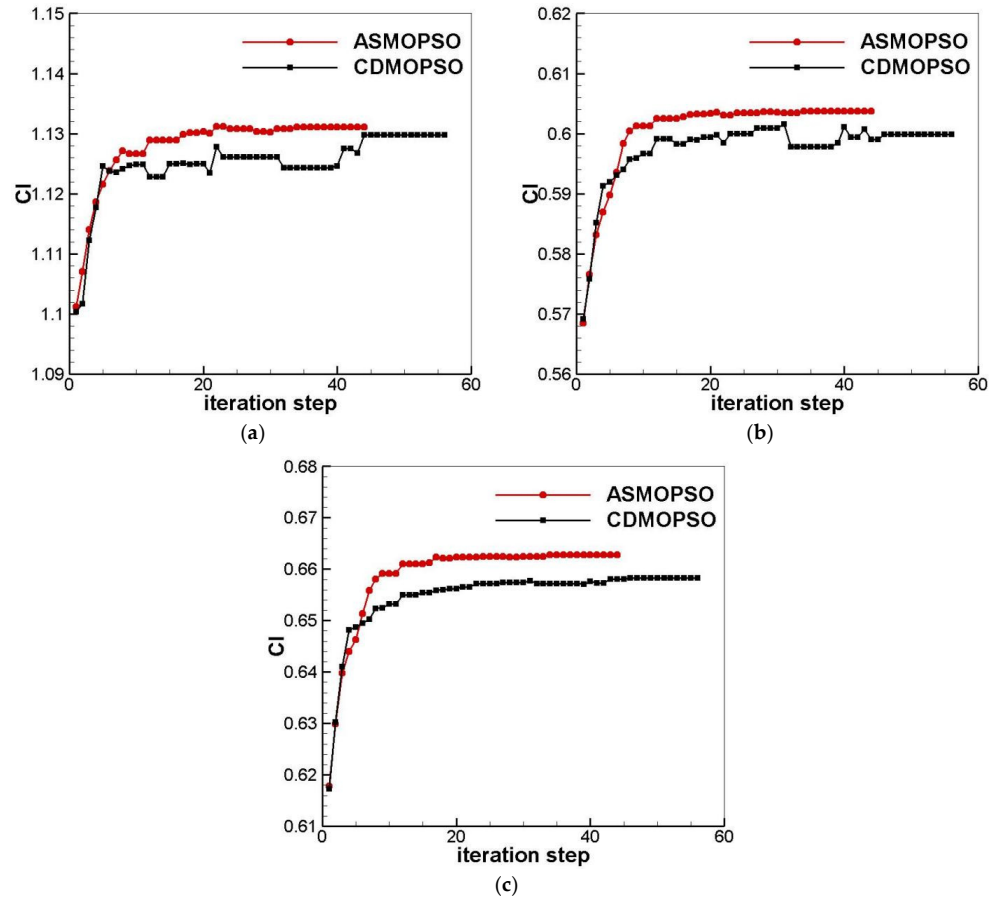


**Figure 13.** Comparison of the performance between the ASMOPSO algorithm and the CDMOPSO algorithm. (a) maneuvering. (b) hovering. (c) forward flight.

In order to pick out a final solution among the non-dominated solutions at each iteration and pick out the optimal solution, a function  $f_{op}$  is defined in Equation (9) with reference to the literature [35–37]. Here  $\omega_1$ ,  $\omega_2$ , and  $\omega_3$  are weight coefficients, which are set to be [1/3, 1/3, and 1/3]. In the Pareto solution set, there are multiple optimal solutions. The solution with the highest value of  $f_{op}$  is taken as the satisfactory solution.

$$f_{op} = \omega_1 \frac{(Cl_m - Cl_m^{\min})}{(Cl_m^{\max} - Cl_m^{\min})} + \omega_2 \frac{(Cl_h - Cl_h^{\min})}{(Cl_h^{\max} - Cl_h^{\min})} + \omega_3 \frac{(Cl_f - Cl_f^{\min})}{(Cl_f^{\max} - Cl_f^{\min})} \quad (9)$$

Table 4 shows the comparison of the optimization results between the CDMOPSO algorithm and the ASMOPSO algorithm. As can be seen, the lift coefficients obtained by the ASMOPSO algorithm are all higher than those obtained by the CDMOPSO algorithm under the three states. Thus, it can be concluded that the ASMOPSO algorithm has a faster convergence rate and obtains better optimization results than the CDMOPSO algorithm for the multi-objective optimization of the rotor airfoil.

**Table 4.** Comparison of the optimization results between the CDMOPSO algorithm and the ASMOPSO algorithm.

	$C_{l_{\text{maneuvering}}}$	$C_{d_{\text{maneuvering}}}$	$C_{l_{\text{hovering}}}$	$C_{d_{\text{hovering}}}$	$C_{l_{\text{forward flight}}}$	$C_{d_{\text{forward flight}}}$
Baseline	1.0668	0.0322	0.5621	0.0121	0.6137	0.0241
CDMOPSO	1.1298	0.0257	0.5998	0.0119	0.6582	0.0241
ASMOPSO	1.1311	0.0259	0.6038	0.0119	0.6628	0.0241

In order to verify the advantages of the DBN surrogate model over the BP surrogate model and the Kriging surrogate model in the multi-objective optimization of the rotor airfoil, three multi-objective optimizations based on the DBN surrogate model, the BP surrogate model and the Kriging surrogate model are performed via the ASMOPSO algorithm. During the optimization process, the EI (expected improvement) infilling criterion is adopted to update the surrogate model in each iteration before the optimization is converged.

Figure 14 shows the optimal values of each objective function by the optimizations employing the DBN surrogate model, the BP surrogate model, and the Kriging surrogate model during the optimization processes. As can be seen, the DBN-based optimization not only converges faster than the BP-based and Kriging-based optimizations but also obtains better results than them.

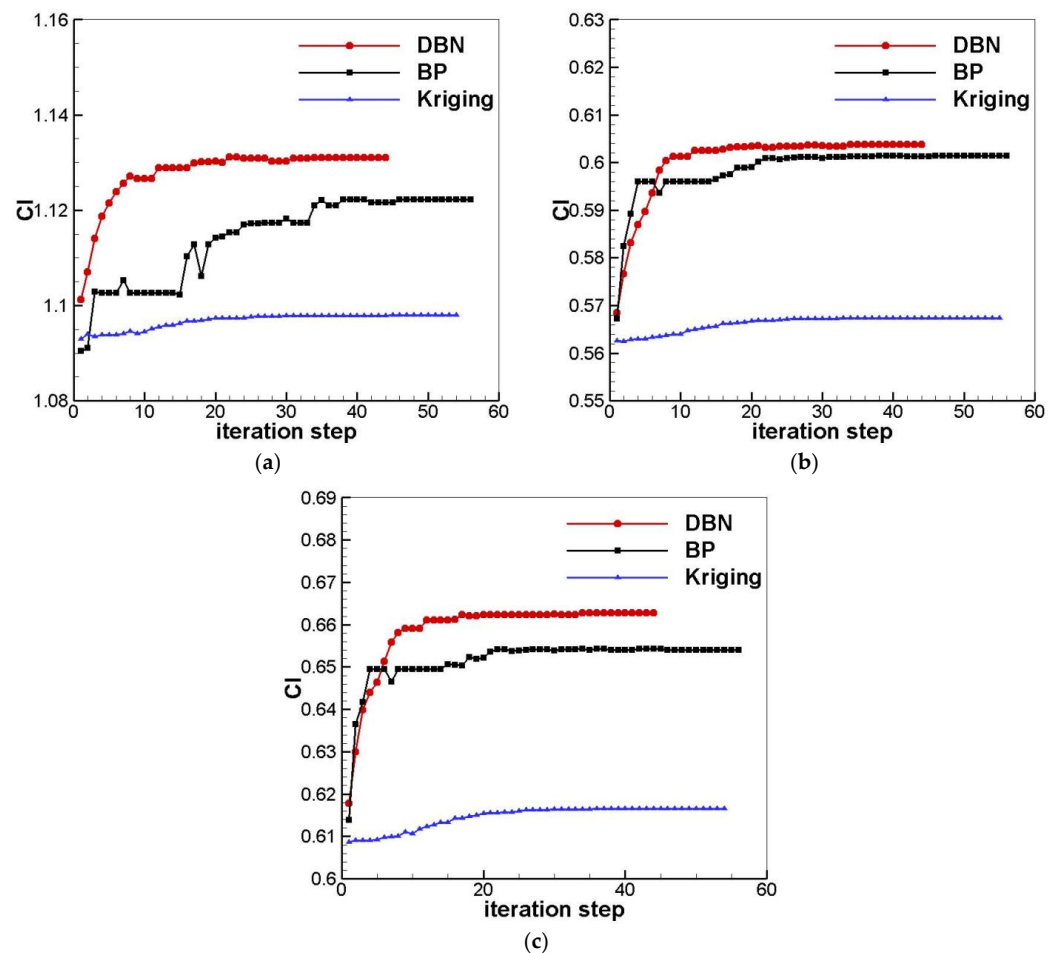


**Figure 14.** Optimal values of the objective functions in each iteration. (a) maneuvering. (b) hovering. (c) forward flight.

Figure 15 shows the finally obtained non-dominated solutions by the optimizations employing the DBN surrogate model, the BP surrogate model, and the Kriging surro-

gate model. The function values presented here are obtained by the predictions of the surrogate models.

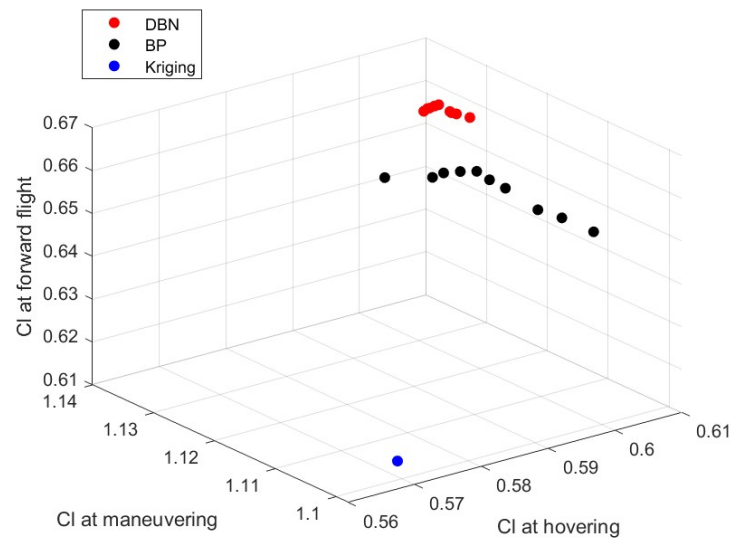


**Figure 15.** Fitness function values of non-dominated particles.

Table 5 shows the computation time and the number of CFD simulation cases during the optimization process for each surrogate model-based optimization. As can be seen, the optimization employing the DBN surrogate model consumes the least computational resources. The aerodynamic parameters of the optimal solutions obtained by the optimizations based on the DBN model, the BP model, and the Kriging model are discussed in Section 4.3.

**Table 5.** Computation time and number of CFD simulation cases during the optimization process.

	Training Time	Number of CFD Simulation Cases
DBN	120 s	344
BP	10 s	356
Kriging	10 s	354
No surrogate model		5000

#### 4.3. CFD Validations for the Optimized Rotor Airfoil

Table 6 shows the predicted aerodynamic parameters of the optimal solutions via the DBN model, the BP model, and the Kriging model compared with the computational results.

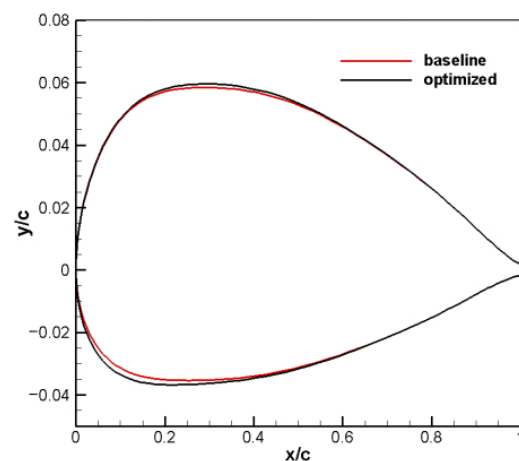
As can be seen from Table 6, the aerodynamic parameters obtained by the DBN surrogate model are very close to those by the CFD simulations, which demonstrates the accuracy of the DBN surrogate model. In addition, both the predicted and computational lift coefficients of the optimal solution obtained by the optimization employing the DBN surrogate model are higher than those by the other two optimizations.

Therefore, the non-dominated solution with the maximum  $f_{op}$  obtained by the DBN surrogate model-based optimization is selected as the final optimized solution. Figure 16 shows the shape of the optimized rotor airfoil compared with that of the baseline rotor airfoil.

From Table 6, the lift coefficients of the optimized rotor airfoil are obviously improved compared with the baseline rotor airfoil, while the drag coefficients of the optimized rotor airfoil are not increased.

**Table 6.** Predicted aerodynamic parameters of the optimal solutions via the DBN-based, the BP-based, and the Kriging-based optimizations compared with the computational results.

	$C_{l_{\text{maneuvering}}}$	$C_{d_{\text{maneuvering}}}$	$C_{l_{\text{hovering}}}$	$C_{d_{\text{hovering}}}$	$C_{l_{\text{forward flight}}}$	$C_{d_{\text{forward flight}}}$
Computational results of the baseline rotor airfoil	1.0668	0.0322	0.5621	0.0121	0.6137	0.0241
Predicted values of DBN-based optimization	1.1311	0.0259	0.6038	0.0119	0.6628	0.0241
Computational values of DBN-based optimization	1.1310	0.0264	0.6040	0.0118	0.6635	0.0240
Errors between computational values and DBN-predicted values [%]	0.01	1.89	0.03	0.85	0.11	0.42
Increment of computational results to the baseline rotor airfoil [%]	6.02	−18.01	7.45	−2.48	8.12	−0.42
Predicted values of BP-based optimization	1.1222	0.0264	0.6014	0.0120	0.6540	0.0241
Computational values of BP-based optimization	1.1203	0.0263	0.5935	0.0118	0.6482	0.0241
Errors between computational values and BP-predicted values [%]	0.17	0.38	1.33	1.70	0.90	0.00
Increment of computational results to the baseline rotor airfoil [%]	5.02	−18.32	5.59	−2.48	5.62	0.00
Predicted values of Kriging-based optimization	1.0983	0.0282	0.5679	0.0119	0.6169	0.0235
Computational values of Kriging-based optimization	1.0952	0.0276	0.5643	0.0116	0.6150	0.0234
Errors between computational values and BP-predicted values [%]	0.28	2.17	0.64	2.59	0.31	0.43
Increment of computational results to the baseline rotor airfoil [%]	2.66	−14.29	0.39	−4.13	0.21	−2.91

**Figure 16.** Comparison of the shape between the optimized rotor airfoil and the baseline rotor airfoil.

In order to verify the improvements of the optimized rotor airfoil on aerodynamic performance, numerical simulations are performed on the optimized airfoil and the baseline airfoil, then the lift curves, drag curves, and lift-drag ratio curves are obtained and compared as shown in Figures 17–19. From the comparisons, the lift coefficients and lift-drag ratios of the optimized rotor airfoil are significantly improved compared with the baseline rotor airfoil, while the drag coefficients of the optimized rotor airfoil are significantly decreased.

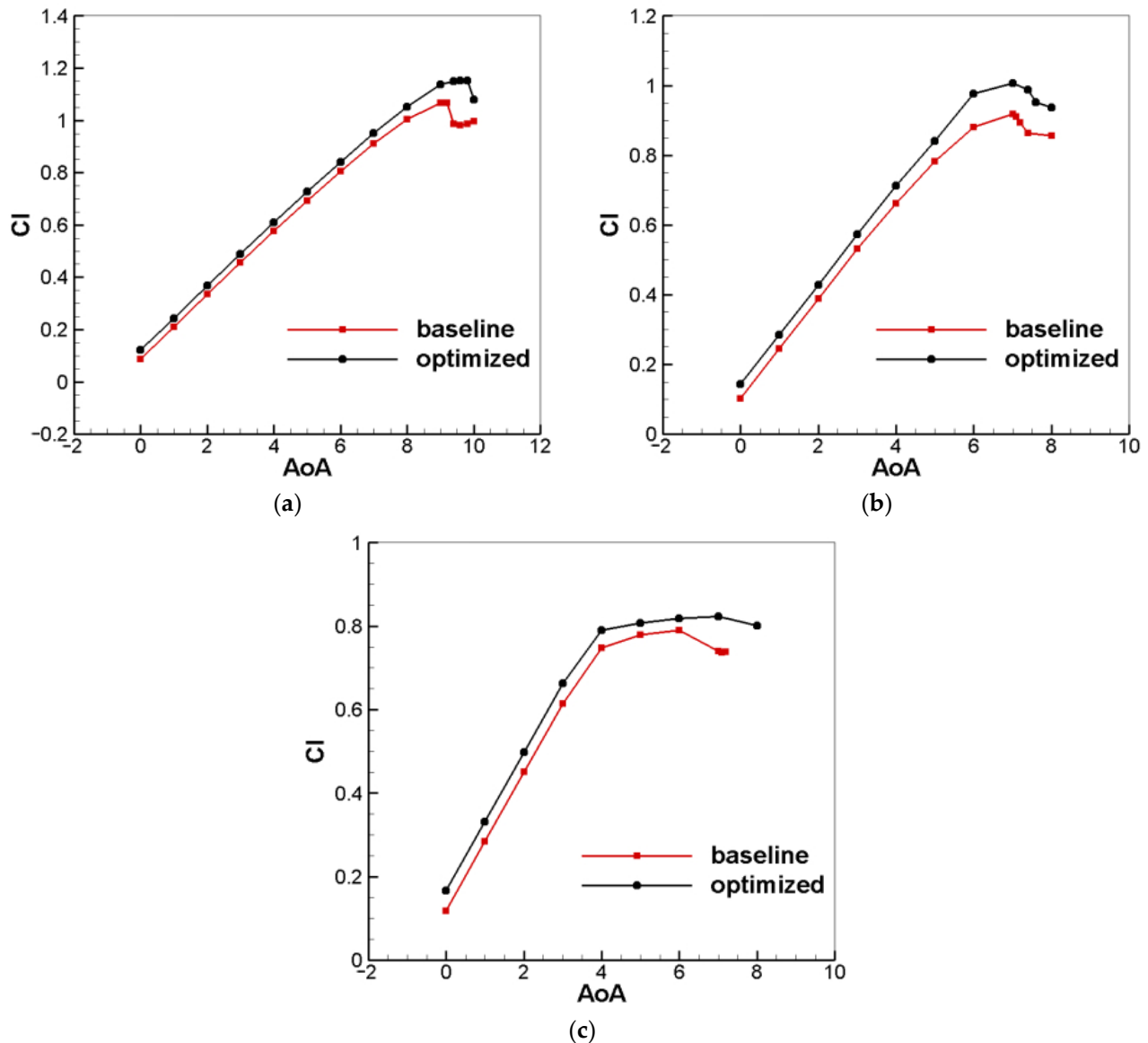


**Figure 17.** Comparison of the lift curves between the optimized rotor airfoil and the baseline rotor airfoil. (a)  $Ma = 0.4$ . (b)  $Ma = 0.6$ . (c)  $Ma = 0.7$ .

Therefore, from the above CFD results of validations, it can be concluded that the DBN surrogate model behaves very well in predicting the aerodynamic parameters during the multi-objective optimization, and the lift performance of the optimized rotor airfoil is improved significantly compared to the baseline rotor airfoil, with the drag coefficients not increased.

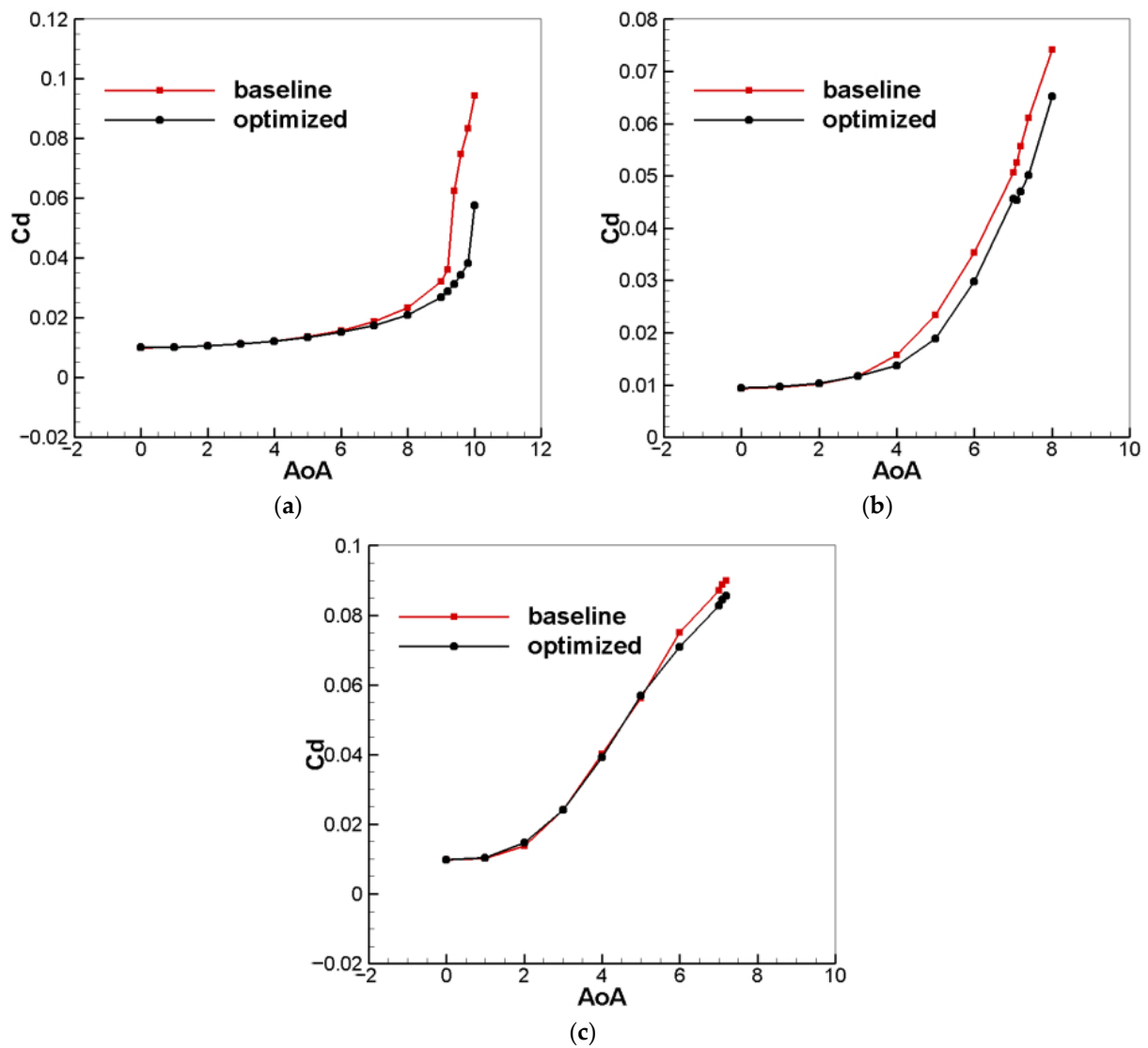


Figure 18. Comparison of the drag curves between the optimized rotor airfoil and the baseline rotor airfoil. (a)  $Ma = 0.4$ . (b)  $Ma = 0.6$ . (c)  $Ma = 0.7$ .

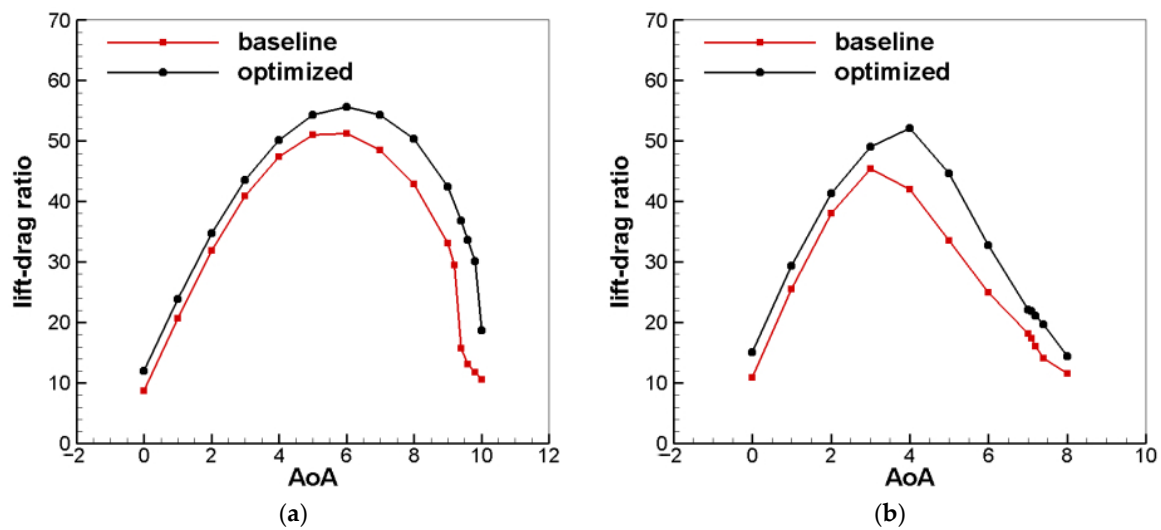
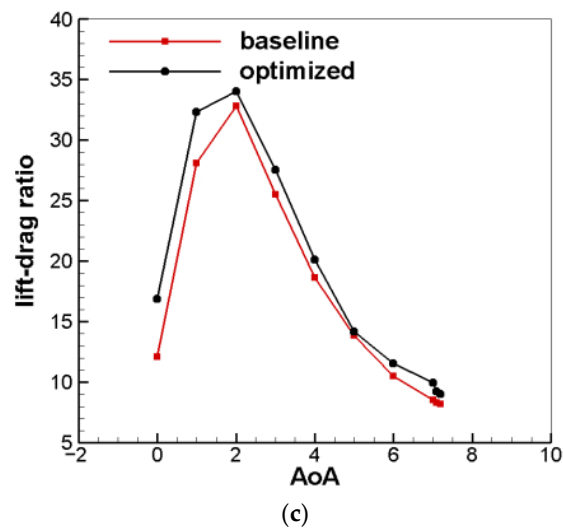


Figure 19. Cont.



**Figure 19.** Comparison of the lift-drag ratio curves between the optimized rotor airfoil and the baseline rotor airfoil. (a)  $Ma = 0.4$ . (b)  $Ma = 0.6$ . (c)  $Ma = 0.7$ .

## 5. Conclusions

In this study, a deep-learning-based multi-objective optimization framework is proposed for the aerodynamic optimization of the rotor airfoil.

A database of rotor airfoils is established with geometric parameters obtained via the CST method and aerodynamic parameters obtained via CFD simulations. Based on the database, a DBN surrogate model is proposed and trained in order to accurately predict the aerodynamic parameters of the rotor airfoils. In order to compare the performance of the DBN surrogate model and the conventional surrogate models, the BP and Kriging surrogate models are trained and tested using the same training and test samples. The average errors of the lift coefficients predicted by the DBN model, BP model, and Kriging model are 0.3416%, 0.7597%, and 0.9482%, respectively, while the average errors of the drag coefficients predicted by the DBN model, BP model, and Kriging model are 1.2875%, 2.5570%, and 2.6005%, respectively. The results indicate that the DBN surrogate model established in this study is highly reliable in predicting aerodynamic parameters for rotor airfoil optimization and is more accurate than the conventional BP surrogate model and Kriging surrogate model.

An improved MOPSO (ASMOPSO) framework is established by employing the DBN surrogate model and introducing  $\alpha$ -stable distribution to improve the convergence rate and global searching ability. For the purpose of verifying the performance of the ASMOPSO algorithm, optimizations employing the CDMOPSO algorithm and the ASMOPSO algorithm are performed, respectively. The optimization based on the CDMOPSO algorithm converges at the 56th step, while the optimization based on the ASMOPSO algorithm converges at the 44th step. The lift coefficients obtained by the ASMOPSO algorithm are all higher than those obtained by the CDMOPSO algorithm under multiple flight states. The comparison results indicate that the ASMOPSO algorithm has a faster convergence rate and obtains better optimization results than the CDMOPSO algorithm does for the multi-objective optimization of the rotor airfoil.

In order to verify the advantages of the DBN surrogate model over the BP surrogate model and the Kriging surrogate model in the multi-objective optimization of the rotor, three multi-objective optimizations based on the DBN surrogate model, the BP surrogate model, and the Kriging surrogate model are performed. The results indicate that both the predicted and computational lift coefficients of the optimal solution obtained by the DBN-based optimization are higher than those obtained by the other two optimizations.

Finally, CFD simulations are performed to validate the aerodynamic performance of the optimized rotor airfoil obtained by the DBN-based optimization. The results indicate

that the lift coefficients are improved by 6.02%, 7.45%, and 8.12% under the maneuvering, hovering, and forward flight states, respectively, with the drag coefficients not increased. Furthermore, the lift curves, drag curves, and lift-drag ratio curves of the optimized airfoil and the baseline airfoil obtained by CFD simulations indicate that the aerodynamic performance of the optimized rotor airfoil is observably improved compared with the baseline rotor airfoil.

**Author Contributions:** Conceptualization, J.T. and G.S.; Methodology, Y.W. and J.T.; Validation, Y.W. and J.T.; Formal Analysis, Y.W.; Investigation, J.T.; Writing—Original Draft Preparation, Y.W. and J.T.; Writing—Review and Editing, J.T. and G.S.; Supervision, G.S.; Funding Acquisition, J.T. All authors have read and agreed to the published version of the manuscript.

**Funding:** This research was co-funded by the Open Project of Rotor Aerodynamics Key Laboratory (No. 2002RAL20200101-2) and the Shanghai Pujiang Program (20PJ1402000).

**Data Availability Statement:** Data are available by contacting the corresponding author.

**Conflicts of Interest:** The authors declare no conflict of interest.

## References

- Desopper, A.; Lafon, P.; CeRoni, P. Ten years of rotor flow studies at ONERA. *J. Am. Helicopter Soc.* **1989**, *34*, 34–41. [\[CrossRef\]](#)
- Raul, V.; Leifsson, L. Surrogate-based aerodynamic shape optimization for delaying airfoil dynamic stall using Kriging regression and infill criteria. *Aerosp. Sci. Technol.* **2021**, *111*, 106555. [\[CrossRef\]](#)
- Vozhdajev, E.; Golovkine, V. Current state-of-the-art of TsAGI studies in the area of helicopter aerodynamics. In Proceedings of the 21st European Rotorcraft Forum, Moscow, Russia, 30 August–1 September 1995.
- Ngoc, A.; Jae, W.; Jung, S. Aerodynamic design optimization of helicopter rotor blades including airfoil shape for hover performance. *Chin. J. Aeronaut.* **2013**, *26*, 1–8.
- Tatossian, C.; Nadarajah, S. Optimum shape design of helicopter rotors in forward flight via control theory. In Proceedings of the 18th AIAA Computational Fluid Dynamics Conference, Miami, FL, USA, 25–28 June 2007.
- Yu, B.; Li, G.; Xie, L.; Wang, F. Dynamic stall optimization design of rotor airfoil based on surrogate model. *J. Zhejiang Univ.* **2020**, *54*, 833–842.
- Yang, H.; Song, W.; Han, Z.; Xu, J. Multi-objective and Multi-constrained Optimization Design for a Helicopter Rotor Airfoil. *Acta Aeronaut. ET Astronaut. Sin.* **2012**, *33*, 1218–1226.
- Wang, Q.; Zhao, Q. Rotor airfoil profile optimization for alleviating dynamic stall characteristics. *Aerosp. Sci. Technol.* **2018**, *72*, 502–515. [\[CrossRef\]](#)
- Yeh, W.; Chuang, M. Using multi-objective genetic algorithm for partner selection in green supply chain problems. *Expert Syst. Appl.* **2010**, *38*, 4244–4253. [\[CrossRef\]](#)
- Goh, C.; Tan, K.; Liu, D.; Chiam, S. A competitive and cooperative co-evolutionary approach to multi-objective particle swarm optimization algorithm design. *Eur. J. Oper. Res.* **2010**, *202*, 42–54. [\[CrossRef\]](#)
- Massaro, A.; Benini, E. Helicopter transonic airfoil shape optimization using hybrid multiobjective strategies. In Proceedings of the International Powered Lift Conference, Philadelphia, PA, USA, 5 October 2010.
- Zhao, K.; Gao, Z.; Huang, J.; Li, Q. Aerodynamic optimization of rotor airfoil based on multi-layer hierarchical constraint method. *Chin. J. Aeronaut.* **2016**, *29*, 1541–1552. [\[CrossRef\]](#)
- Koning, W.; Romander, E.; Johnson, W. Optimization of low Reynolds number airfoils for Martian rotor applications using an evolutionary algorithm. In Proceedings of the AIAA Scitech 2020 Forum, Orlando, FL, USA, 6–10 January 2020.
- Zhang, W.; Sun, J.; Wang, L.; Jie, W.; Long, H. Rotor airfoil aerodynamic design method and wind tunnel test verification. *Chin. J. Aeronaut.* **2020**, *33*, 2123–2132. [\[CrossRef\]](#)
- Cai, L. Research on the multi-objective case based on improved genetic algorithms. *Comput. Engin. Sci.* **2008**, *30*, 75–77.
- Fan, H.; Zhan, H.; Cheng, S.; Mi, B. Research and Application of Multi-Objective Particle Swarm Optimization Algorithm Based on  $\alpha$ -Stable Distribution. *J. Northwest. Polytech. Univ.* **2019**, *37*, 232–241. [\[CrossRef\]](#)
- Dey, S.; Mukhopadhyay, T.; Adhikari, S. Stochastic free vibration analyses of composite shallow doubly curved shells—A Kriging model approach. *Compos. Part B Eng.* **2015**, *70*, 99–112. [\[CrossRef\]](#)
- Shi, H.; Yang, J.; Ding, M.; Wang, J. A Short-term Wind Power Prediction Method Based on Wavelet Decomposition and BP Neural Network. *Autom. Electr. Power. Syst.* **2011**, *35*, 44–48.
- Shen, D.; Peng, B.; Li, Z.; Gong, Y.; Li, P. Research on Aerodynamic Surrogate Modeling for Launch Vehicle Collaborative Optimization. *Astronaut. Syst. Eng. Technol.* **2020**, *4*, 44–50.
- Tao, J.; Sun, G. An artificial neural network approach for aerodynamic performance retention in airframe noise reduction design of a 3D swept wing model. *Chin. J. Aeronaut.* **2016**, *29*, 1213–1225. [\[CrossRef\]](#)
- Kim, T.; Kim, S.; Lim, J.; Jee, S. Numerical investigation of compressibility effect on dynamic stall. *Aerosp. Sci. Technol.* **2020**, *105*, 105918. [\[CrossRef\]](#)

22. Harris, C. *Two-Dimensional Aerodynamic Characteristics of the NACA 0012 Airfoil in the Langley 8 Foot Transonic Pressure Tunnel*; NASA Technical Report; NASA: Washington, DC, USA, 1981.
23. Ladson, C. *Effects of Independent Variation of Mach and Reynolds Numbers on the Low-Speed Aerodynamic Characteristics of the NACA 0012 Airfoil Section*; NASA Technical Memorandum 4074; NASA: Washington, DC, USA, 1988.
24. HyeonWook, L.; Hyoungjin, K. Multi-objective airfoil shape optimization using an adaptive hybrid evolutionary algorithm. *Aerosp. Sci. Technol.* **2019**, *87*, 141–153.
25. Yang, S.; Lee, S.; Yee, K. Inverse design optimization framework via a two-step deep learning approach: Application to a wind turbine airfoil. *Eng. Comput.* **2022**, *39*, 2239–2255. [[CrossRef](#)]
26. Che, C.; Wang, H.; Fu, Q.; Ni, X. Combining multiple deep learning algorithms for prognostic and health management of aircraft. *Aerosp. Sci. Technol.* **2019**, *94*, 105423. [[CrossRef](#)]
27. Jin, R.; Rocco, P.; Geng, Y. Cartesian trajectory planning of space robots using a multi-objective optimization. *Aerosp. Sci. Technol.* **2021**, *108*, 106360. [[CrossRef](#)]
28. Carlos, C.; Maximino, S. MOPSO: A proposal for multiple objective particle swarm optimization. *IEEE. Comput. Soc.* **2002**, *2*, 1051–1065.
29. Molina-Muñoz, J.; Mora-Valencia, A.; Perote, J. Market-crash forecasting based on the dynamics of the alpha-stable distribution. *Phys. A* **2020**, *557*, 124876. [[CrossRef](#)]
30. Li, J.; Quan, H.; Cui, P. Parameter estimation for skewed  $\alpha$ -stable distribution based on PSO. *Chin. J. Radio Sci.* **2013**, *28*, 163–168.
31. Zhan, D.; Cheng, Y.; Liu, J. Expected Improvement Matrix-Based Infill Criteria for Expensive Multiobjective Optimization. *IEEE Trans. Evol. Comput.* **2017**, *21*, 956–975. [[CrossRef](#)]
32. Chae, S.; Yee, K.; Yang, C.; Aoyama, T.; Jeong, S.; Obayashi, S. Helicopter rotor shape optimization for the improvement of aeroacoustic performance in hover. *J. Aircr.* **2010**, *47*, 1770–1783. [[CrossRef](#)]
33. Yang, S.; Yee, K. Design rule extraction using multi-fidelity surrogate model for unmanned combat aerial vehicles. *J. Aircr.* **2022**, *59*, 977–991. [[CrossRef](#)]
34. Afzal, A.; Kim, K.; Seo, J. Effects of Latin hypercube sampling on surrogate modeling and optimization. *Int. J. Fluid Mach. Syst.* **2017**, *10*, 240–253. [[CrossRef](#)]
35. Paraskevopoulos, A.; Dallas, P.; Siakavara, K.; Sotirios, K. Cognitive Radio Engine Design for IoT Using Real-Coded Biogeography-Based Optimization and Fuzzy Decision Making. *Wirel. Pers. Commun.* **2017**, *97*, 1813–1833. [[CrossRef](#)]
36. Mohammad, R.; Jafar, R.; Meisam, B.; Parviz, M. Multi-objective collaborative multidisciplinary design optimization using particle swarm techniques and fuzzy decision making. *Inst. Mech. Eng.* **2012**, *226*, 2281–2295.
37. Cen, W. Optimization of Production Equipment Layout Based on Fuzzy Decision and Evolutionary Algorithm. *Int. J. Decis. Support. Syst. Technol.* **2019**, *11*, 13–29.

**Disclaimer/Publisher’s Note:** The statements, opinions and data contained in all publications are solely those of the individual author(s) and contributor(s) and not of MDPI and/or the editor(s). MDPI and/or the editor(s) disclaim responsibility for any injury to people or property resulting from any ideas, methods, instructions or products referred to in the content.